STUDIA UBB CHEMIA, LXX, 3, 2025 (p. 65-84)
(RECOMMENDED CITATION)
DOI:10.24193/subbchem.2025.3.05

NANO-STRUCTURED Nd-Fe-B THIN FILMS DEPOSITED ON GLASS SUBSTRATE BY FLASH EVAPORATION METHOD

Ana-Maria POPESCU[a]*, Mihai ANASTASESCU[a], Jose CALDERON MORENO[a], Elena Ionela NEACSU[a], Olga DEMIDENKO MINCHUKOVA[b], Kazimir YANUSHKEVICH[b(†)], Virgil CONSTANTIN[a]*

ABSTRACT. Nd-Fe-B nanostructured thin layers have been growth on the glass substrate by the "flash" evaporation (FE) method. The microscopic and surface structure analysis of the Nd-Fe-B thin films investigated by X-ray diffraction (XRD), scanning electron microscopy (SEM), atomic force microscopy (AFM) and X-ray photoelectron spectroscopy (XPS) demonstrate these thin films to be nanostructured.The temperature dependence of the specific magnetization of the films in the 80 ≤ T ≤ 800 K range, measured by the ponderomotive method showed that the magnetization of the Nd-Fe-B nanostructured thin films before corrosion did not exceed 85 $A \cdot m^2 \cdot kg^{-1}$ at 77 K. In such Nd-Fe-B nano thin films the long-range structural order is destroyed. After corrosive action on the thin films, their specific magnetization value increased to 140-155 $A \cdot m^2 \cdot kg^{-1}$, most probably because of the formation of Fe_3O_4 (iron oxide) and the presence of free iron ions on the surface of the nanometric Nd-Fe-B layer upon heating the samples to 1050 K. XPS spectra confirmed the presence of Fe_3O_4, FeOOH and $Nd(OH)_3$.

Keywords: *nanostructured thin film, NdFeB thin films; microstructure; characterization of thin films; thin film surface analysis; nanomagnetic properties of NdFeB thin films.*

[a] *Romanian Academy, "Ilie Murgulescu" Institute of Physical Chemistry, Laboratory of Electrochemistry and Corrosion, 202 Splaiul Independentei, 060021, Bucharest, Romania*
[b] *Scientific-Practical Materials Research Center NAS, P. Broski Str.19, Minsk, Belarus*
* *Corresponding authors: popescuamj@yahoo.com, virgilconstantin@yahoo.com*

INTRODUCTION

Permanent Nd-Fe-B magnets and products based on them are currently widely used in the development of many industries [1-7]. Application of this class of magnets opens the perspective of creating products with fundamentally new technical capabilities. It is already known that, Nd-Fe-B magnets span a wide range of magnetic properties and application requirements due to large values of the coercive force and residual magnetization. A highly sought-after target of present work is to provide transparent nano-magnets based on quenched Nd-Fe-B permanent magnets for some miniature engineering products. The structural and magnetic properties of Nd-Fe-B thin films represent a subject of growing scientific interest due to the wide range of applications especially on MEMS (micro-mechanical systems), MES (micro-electronical systems) and MMD (micro-magnetic devices). There are a lot of studies on Nd-Fe-B thin films [8-12]. This interest determines the relevance of studying the properties of Nd-Fe-B nanocrystalline thin films [13-15]. In this paper we will present the structure, morphology, surface chemistry and magnetic properties of Nd-Fe-B nano-structured thin films evaporated on glass substrate by the “flash” method (FM). The motivation of this investigation is based on the challenge to analyze information on the nano-structured Nd-Fe-B film sample deposited by FM on glass, as we did not found any other study in the literature.

RESULTS AND DISCUSSION

1.Thin film characterization

The X-ray analysis of precursor powder used for thin film production from the permanent magnets showed that their crystal structure corresponds to the tetragonal $R4_2/mnm$ space group of $Nd_2Fe_{14}B$ compound (Fig. 1) [16]. Results of the crystal structure study of Nd-Fe-B nanolayers in CuK_α-radiation revealed that for all the three prepared samples (Fig. 1 a, b, c), their structure is nano-crystalline. The film thickness of sample (0.2 mg) is too small and Bragg peaks related with the film cannot be detected. Increasing a film thickness, intensity of the strongest Bragg peak increases however the peak are much wider then for precursor materials. It might indicate on small crystalline size and stress in film as well. Origins of (physical) line broadening are numerous. In general any lattice imperfections will cause additional line broadening, which can be dependent and independent on the reflection order: if a crystal is broken into smaller incoherently diffracting domains by dislocation arrays (small-angle boundaries), stacking faults, twins, or other extended imperfections, then size broadening occurs; dislocations, vacancies, interstitials, substitutionals, and similar defects lead to microstrain broadening. From the nature of the lattice

imperfections noted above follows, that both effects are interconnected. For example dislocations cause lattice strain but also arrange into boundaries between incoherently diffracting domains resulting in crystallite size broadening. This is one of the reasons why any interpretation of the underlaying physics of broadening is difficult. XRD data that was introduced in the analysis software program TOPAS 5 and crystallite size was calculated. So, calculation give a crystallite size of about 1.203 nm for sample 0.2 mg, 2.85 nm for sample 0.3 mg and 2.95 nm for sample 0.7 mg. For sample 0.2mg (Fig.1 b) it is difficult to apply Scherrer formula on the XRD pattern, but for the other samples (Fig.1 c, d) which are clearly nanocrystalline we calculate the crystallite size (D) for the peak at 28° and the obtained values are: 2.04 nm for sample 0.3mg and 2.73 nm for sample 0.7mg. Those results are of the same order of magnitude with thedata obtained by TOPAS 5 calculation.

The thickness of these nano-films calculated from the density and film area were as follows: 0.2 mg (sample 1) – 110 ± 5 nm, 0.3 mg (sample 2) – 150 ± 5 nm and 0.7 mg (sample 3) – 360 ± 5 nm. For density value we used a literature one for $Nd_2Fe_{14}B$ constant magnet (7.4 g/cm^3). In our case the process the thin films formation can be described as follows. $Nd_2Fe_{14}B$ vaporized mass is the only one variable of the deposition process influencing the films thickness and nano-structures shape and size. The alloy vapours in contact with the glass slide forms germination spots and the nanoparticles grew through homogeneous crystallization. In consequence:

- low density vapours (0.2 mg vaporized material) generates a lot of small germination spots which further grows as numerous small nanoparticles;
- mean density vapours (0.3 mg vaporized material) generates a lot of germination spots which grows developing numerous nanoparticles slightly bigger than previous ones. A small fusion between two adjacent germination spots might occur explaining the appearance of bigger formations;
- high density vapours (0.7 mg vaporized material) generates a lot of germination spots. The higher vapour density facilitates the faster homogeneous growth developing strong nano-particles that partly fuses each other becoming nano-structural clusters.

The XRD pattern of a NdFeB magnet corroded in a NaCl solution will show the disappearance of the original $Nd_2Fe_{14}B$ phase peaks, replaced by peaks associated with corrosion products like iron and neodymium oxides and hydroxides. The corrosion process in NaCl solution preferentially attacks the Nd-rich phases, leading to the formation of these corrosion products. In fact corrosion can only change the surface of the sample. In Fig. 1 e is depicted XRD patterns of the corrosion product after 10 minutes in aq. solution 3.5 wt. % NaCl. The analysis shows that corrosion product contains Lepidocrocite [17], Goethite [18] and $Nd(OH)_3$ [19]. The average size of crystallite (D), calculated with Sherrer formula for the main peaks in Fig.1 e were 7.68 nm for FeOOH and 4.68 nm for $Nd(OH)_3$.

In fact XRD probes deeper than the surface layer (~1–10 μm), but corrosion products form in an ultra-thin surface layer (~10–100 nm). Corrosion products (Nd_2O_3, Fe_2O_3, B_2O_3) are often poorly crystalline or amorphous in early-stage corrosion. Surface roughening may slightly broaden XRD peaks, but not always enough to shift or replace them [20]. In fact **XRD isn't suitable** for detecting surface-limited corrosion on $Nd_2Fe_{14}B$ thin film magnets exposed to 3.5 wt. % NaCl and that is why we choosed the XPS experiments for surface study.

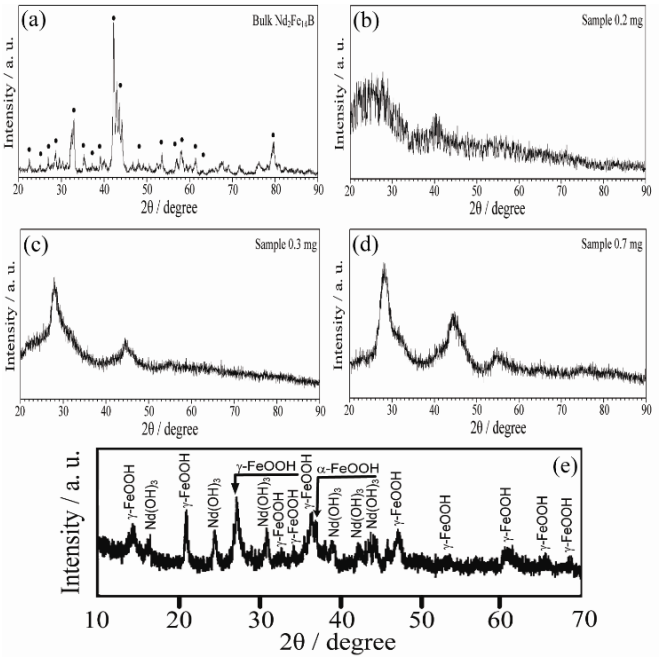

Figure 1. a) XRD pattern of bulk Nd-Fe-B; b-d) XRD pattern of as-deposited Nd-Fe-B thin films, e) XRD patterns of the corrosion product after 10 minutes in aq. solution 3.5 wt. % NaCl.

SEM micrographs obtained on the three Nd-Fe-B thin films on glass (Fig. 2) revealed homogeneous and dense films with a granulated surface texture, indicating a polycrystalline structure of equiaxed nanosized grains. The isolated grains sticking out of the film give a good indication of the particle size. Sample 0.2 mg (Fig. 2 a-b) show grains sized 50-80 nm, sample 0.3 mg (Fig. 2 c-d) show bigger grains of 70-120 nm. Sample 0.7 mg (Fig. 2e) shows a distinct feature that is the formation of columnar agglomerates of hundreds of nms or even micron-size, about one order of magnitude higher than the isolated particles observed in samples 1 and 2 corresponding to deposition of 0.2 and 0.3 mg, respectively.

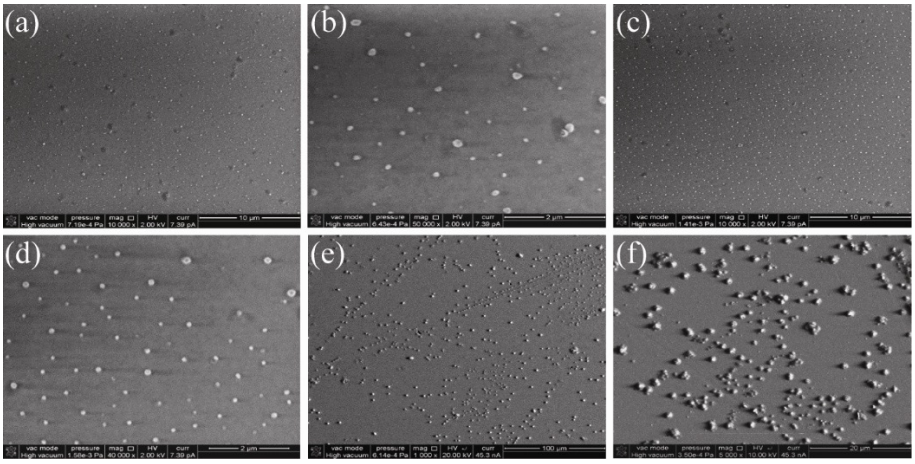

Figure 2. SEM micrographs of different magnifications of the nanostructured thin films in sample 1 (0.2 mg): a) 10 000 x b) 50 000 x; sample 2 (0.3 mg): c) 10 000 x d) 40 000 x; sample 3 (0.7 mg): e) 1 000 x f) 5 000 x.

Atomic force microscopy (AFM) measurements were used to study the surface microstructure of the Nd-Fe-B thin films in higher details, before and after corrosion tests, and the results are shown in Fig. 3.

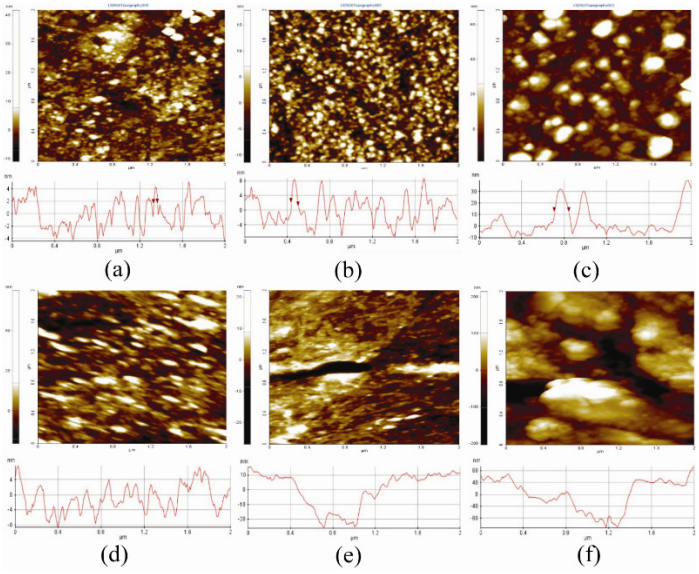

Figure 3. 2D AFM images (2x2 μm^2) and line profiles of NdFeB nanostructured thin films, before: a) sample 1-0.2 mg; b) sample 2-0.3 mg; c) sample 3-0.7 mg and after corrosion tests: d) sample 1-0.2 mg; e) sample 2-0.3 mg; f) sample 3-0.7 mg

While SEM images were scanned over larger areas (Fig. 2), details on the morphology of the sample at nanometric scale, were obtained from the AFM images taken over 2×2 μm^2. Taking into considerations the microstructural aspects reveal by both SEM and AFM, it can be observed that sample 1 exhibit the beginning of a particles structure formation, which due to thelow density vapours (0.2 mg vaporized material) generates random small particles growth sites, further leading to a random appearance of distinct surface particles (Fig. 3 a). Fig. 3b exhibit a homogeneous structure of individual surface particles, well defined, due to the increased vapours density (0.3 mg vaporized material) which generates a large number of germination sites, which further develop a uniform structure of nanoparticles, with diameters slightly bigger. The highest vapour density in this series (0.7 mg vaporized material) leads to a fast interaction between the particles (high diffusion rate) favouring the particles fusion, explaining the appearance of large particles – Fig 3c (in form of material clusters at larger scales). The information regarding the films microstructure (thickness and grains dimensions) is summarized in Fig 4a.

AFM measurements were also performed after corrosion experiments and the images recorded for samples 1, 2 and 3 with 0.2 mg, 0.3 mg and 0.7 mg deposition weights, are presented in Fig 3 d-f. It can be noticed the appearance of the distinctive marks of the corrosion process as pits and ditches, and the distortion of the previously formed particles.

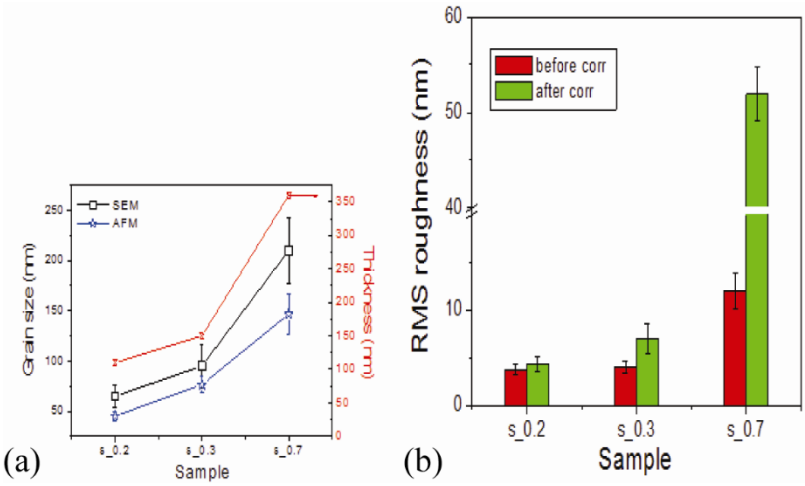

Figure 4. Thickness and grains size from SEM and AFM (a) Roughness histograms for the sample 1- 0.2 mg, sample 2- 0.3 mg and sample 3- 0.7 mg (at the scale of 2x2 μm^2) before and after corrosion tests (b).

In line with the results obtained before corrosion experiments, and with the SEM observations, a similar trend in roughness behavior (before and after corrosion tests) could be observed in Fig. 4b, in which lower value of roughness are found for samples 0.2 and 0.3 mg in comparison with sample 0.7. However, typical pattern of corrosion could be observed on sample 0.7, in agreement with SEM (as shown later), in forms of deep cracks of hundred of nm (as well as in the AFM image recorded at the scale of 8x8 microns).

A comparison between XRD and AFM measurements shows that a 33 % increase in crystallite size for the samples 0.3 mg and 0.7 mg (from 2.05 to 2.73 nm) corresponds to a 175% increase in surface roughness (from 4.45 to 12.25 nm). This indicates that even modest increases in crystallite size can result in significant changes in surface morphology, likely due to grain coalescence and emerging surface topography. Thus, while crystallite size and roughness are distinct properties, their evolution may be linked under certain processing or environmental conditions.

In order to obtain surface chemistry information, X-ray photoelectron spectroscopy (XPS) was performed on Nd-Fe-B nanostructured thin films that had been exposed to atmosphere. The survey spectra were collected over a binding energy range of 0-1200 eV. Depth profile XPS was aquired using an Ar ion gun operated at 2 KeV (2x2)mm scaning area for 1 minute and 5 minutes time sputtering. Referring to Fig. 5, elemental analysis of characteristic binding energies confirms the presence of neodymium (Nd4d, 3d5), praseodymium (Pr3d), oxygen (O2s, 1s), sodium (Na2s,1s, KLL), carbon (C1s), iron (Fe3s, 2p,LMM) and boron (B1s). It is already known that rare earth metals can not be completely separated, so Pr is an impurity of Nd. The presence of a peak corresponding to C on the XPS spectra is due to environmental contamination or handling of the samples, while that of Na peak is due to the glass substrate because the Nd-Fe-B are very thin (nano films). The thickness of the deposited film was estimated at ~25nm by theory, into account the sputter rate [20] and the inelastic mean free path (imfp) ~ 5 nm for Fe 2p transition. This, calculation leads us to an overall thicken of ~ 25 nm. As for the O peak, this might results from the adsorbed oxygen during air exposure. The Na(KLL), Fe(LMM), Fe(LMM1) and Fe(LMM2) lines represent Auger transitions.

It has already been shown by Mao et al [21] that the peaks of Fe and Nd are present in the XPS spectrum of Nd-Fe-B in the Nd-rich phase. All XPS spectral peaks were fitted with PhI Multipack 9.1.0.9. software using Gaussian-Lorentian line shapes. Deconvolution of the peaks is necessary in order to identify correctly all the peaks present and to obtain quantitative data pertaining to relative concentrations. However, this step is quite challenging and nearly impossible considering the number of constituents present within the alloy and the amount of overlapping that occurs between characteristic binding energies.

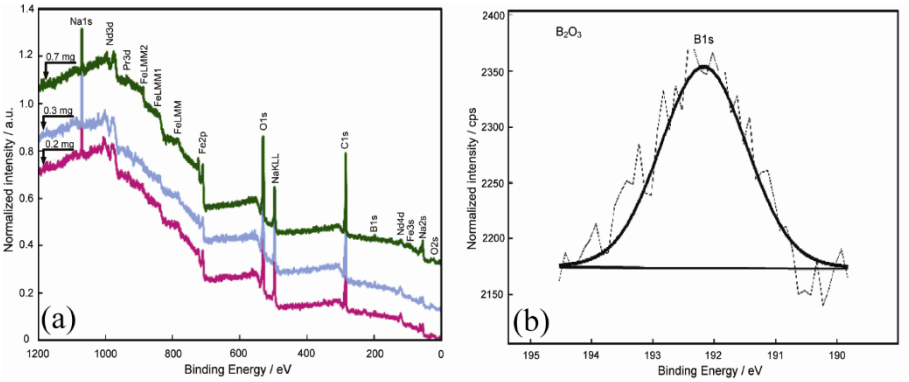

Figure 5. a) Wide scan XPS spectra for the Nd-Fe-B nano-structured thin films: sample 1-0.2 mg (bottom spectrum); sample 2-0.3 mg (middle spectrum); sample 3-0.7 mg (top spectrum); b) B1s deconvoluted spectrum.

To further determine the film components, high-resolution XPS spectra of C1s, O1s, B1s, Nd 3d, Nd 4d and Fe 2p regions were recorded. The spectra were fitted using Gaussian-Lorentzian curves modified by a tail function, after back subtraction following the Shirley procedure [22]. The concentrations of Nd, Fe and B in the three studied samples were quantified using high-resolution spectra of O2s, C1s, Nd3d, Nd4d, Fe2p and B1s.

The obtained results are presented in Table 1. It is appropriate to note here that all the calculations were performed assuming that the samples were homogeneous within the XPS detected volume. We have to emphasize that the errors in our quantitative analysis (relative concentrations) were estimated to be in the range of ± 10 %, while the accuracy for Binding Energies (BEs) assignments was found to be ± 0.2 eV. The accuray of the quantitative analysis (rel.conc. or values the BEs) was estimated by manufacture Company (ULVAC-PHI) [23].

The high-resolution spectra of B1s are very noisy (see Fig. 5b) because concentration of B in the alloy is very low. However, XPS analysis identified the oxidized state, namely B_2O_3. The dotted spectrum is the experimental curve, the line spectrum is the theoretical deconvolution.

The deconvoluted spectra for the $Nd3d_{5/2}$, indicates the presence of stable neodymium oxide, Nd_2O_3 at a binding energy of 982.5 eV (Fig. 6a). The Nd 4d transition indicates that the volume of the “nano film” gives the signal (Fig. 6b). The presence of a number of oxidation states in transition metals can give several transitions corresponding to a particular element as seen in this case for Nd.

Table 1. The relative elemental composition of Nd, Fe, B, C and O in wt.% in the three thin film Nd-Fe-B samples quantified by using high-resolution spectra of O2s, C1s, Nd3d, Nd4d, Fe2p and B1s (see Section 1).

Deposited wt.	Element composition* (wt.%)				
	C	O	Nd	Fe	B
1 (0.2 mg)	1.47	10.47	35.28	52.59	0.18
2 (0.3 mg)	0.48	10.91	38.21	49.78	0.60
3 (0.7 mg)	0.28	30.51	31.56	37.55	0.08

* Estimated errors in the reported values of relative elemental concentrations in the three Nd-Fe-B thin films are ± 10 %

In the case of iron oxides (FeO, Fe_2O_3), the Fe_2O_3 (Fig.6c inset) could be reduced to Fe_3O_4 by Ar^+ sputtering in XPS analysis, or by oxidation during a corrosion process [24-26]. So one can see from the high resolution spectra (Fig.5b and Fig. 6) that all elements (Nd, Fe, B) of the nano-films are present in their oxidized form (B_2O_3, Nd_2O_3, Fe_2O_3) in the Nd-Fe-B nano-films. Table 2 summarizes the corresponding binding energies determined from the XPS spectra.

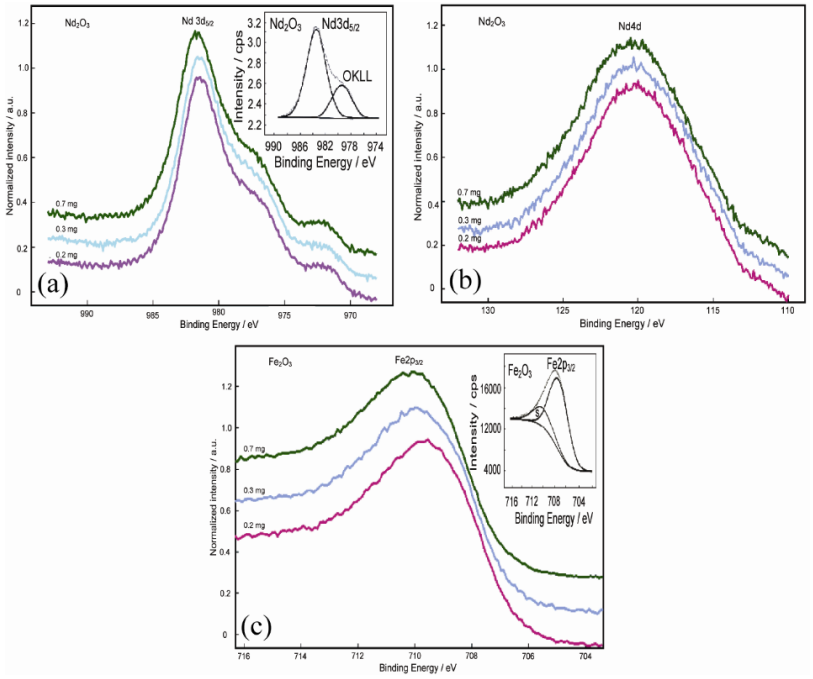

Figure 6. High resolution XPS spectra for: a) Nd3d (inset - the deconvoluted spectrum); b) Nd4d; c) Fe2p (inset - the deconvoluted spectrum).

Table 2. Calculated binding energies from XPS spectra for the initial Nd-Fe-B nanostructured thin films.

Deposited wt.	Binding energies* - B.E. (eV)			
	Nd $3d_{5/2}$	Nd 4d	Fe $2p_{3/2}$	B 1s
1 (0.2 mg)	983.4	121.2	709.5	192.1
2 (0.3 mg)	982.5	122.0	710.0	192.3
3 (0.7 mg)	982.8	122.3	710.2	192.0

* Estimated uncertainties in the reported calculated values of binding energies in the three Nd-Fe-B thin films are ± 0.2 eV.

2. Magnetic properties

Results of average specific magnetization (σ) measured as a function of temperature for three transparent films with d < 100 nm thickness are presented in Fig. 7. This figure shows that at ~ 100 K the nano-films specific magnetization is 85 ± 0.005 $A \cdot m^2 \cdot kg^{-1}$. Films heating to T ~ 750 K during the specific magnetization measurement changes the magnetic state of the films, leading to a decrease in the specific magnetization as seen in Fig. 7. Continuous reduction in the specific magnetization of nanostructured films from 77 K to 750K may be caused by the changing chemical composition of the thin films. The Curie temperature of all studied thin films is almost the same as the initial powders (about 580 K). The Curie temperature is determined from extrapolation of the linear part of $\sigma^2 = f(T)$ dependence to x axis.

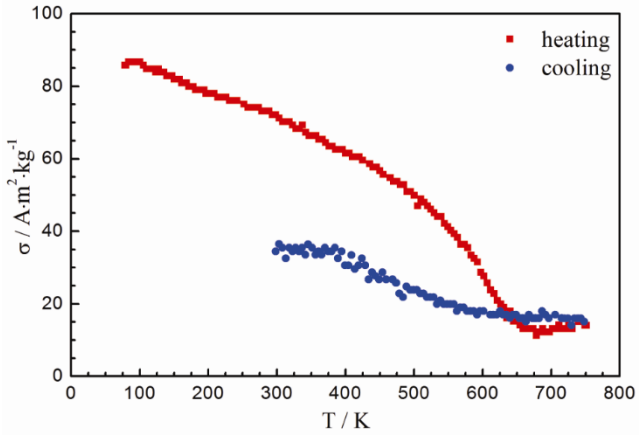

Figure 7. Temperature dependence of average specific magnetization before corrosion action of Nd-Fe-B nanostructured thin films of thickness, d < 100 nm.

3. Morphology, magnetic and surface properties of the nano-structured thin films after the corrosion test

It was established that the corrosion action most noticeably changes the magnetic state of nanoscale films.

Even if the samples were so thin (nanostructed) which do not justify subjecting them to a corrosion study, we performed rapid potentiodynamic corrosion tests in a 3.5 wt. % NaCl aerated solution at 25±0.5° C. By the open circuit potential test (OCP), zero current potentials were determined as follows: for sample 1 (0.2 mg deposition weight), E_{OCP}= -0.425 V; for sample 2 (0.3 mg deposition weight), E_{OCP}= -0.045 V; and for sample 3 (0.7 mg deposition weight), E_{OCP}= -0.397 V. But we observed the rapid dissolution of the samples (too thin) and so neither Tafel plots, nor the calculated kinetic parameters of corrosion process could not be measured. In this case, we limited ourselves to establishing the morphology and surface condition of the nano-structured Nd-Fe-B films after the corrosion process.

SEM measurements of the samples after corrosion in 3.5 wt.% NaCl revealed very significant morphological changes and confirmed the destruction of films, as can be seen in Fig. 8.

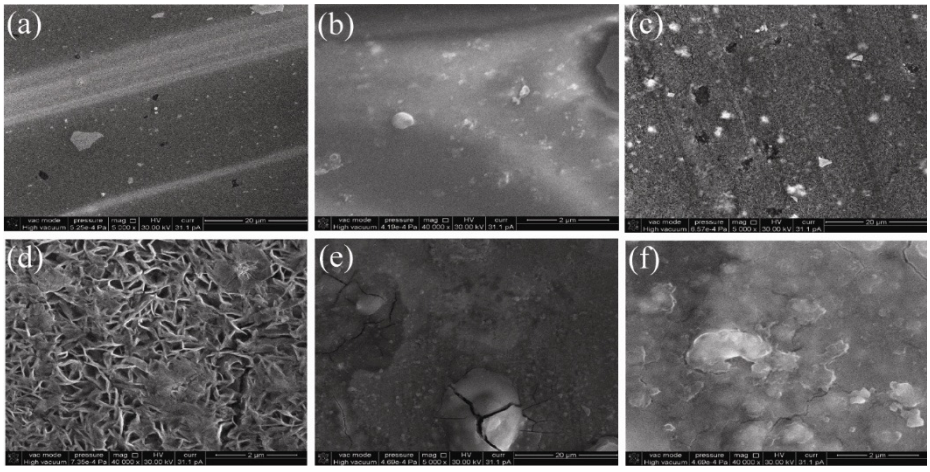

Figure 8. SEM images of different magnification of the Nd-Fe-B films after corrosion process in 3.5 wt. % NaCl. Sample 1 (0.2 mg): a) 5 000 x and b) 40 000 x; sample 2 (0.3 mg): c) 5 000 x and d) 40 000 x; sample 3 (0.7 mg): e) 5 000 x and f) 40 000 x.

Corrosion process leads to the disappearance of the 0.2 mg nanostructured film and to formation of cracks and delaminated surface in the 0.7 mg film. Surprisingly however, sample 2 (0.3 mg) showed the formation

of novel characteristic microstructures of intersecting nanowalls, with thickness of around 50 nm, growing perpendicularly to the plane of the film as can be seen from the structure shown at a higher magnification of 100 000 x in Fig. 9. In this figure both acicular grains and tabular scales are observed and as γ – FeOOH (Lepidocrocite) forms flattened scales (tabular crystals), this confirms the XRD data from Figure 1e.

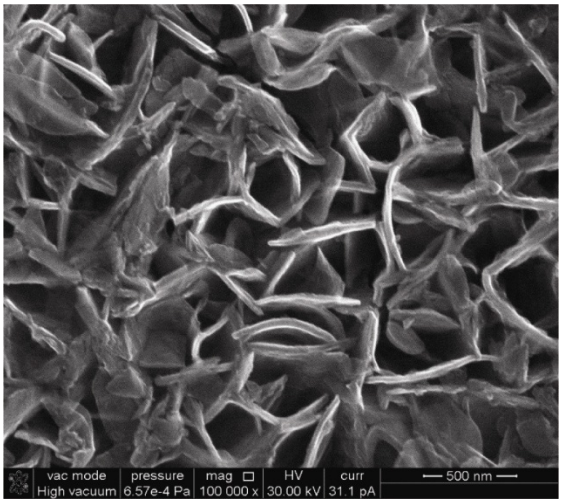

Figure 9. SEM imagesat a higher magnification of 100 000 x providing detail of the nanowalls grown perpendicularly to the sample 2- 0.3 mg after corrosion.

By analyzing the σ = f (T) temperature dependence of Nd-Fe-B nanoscale films after exposure to oxidative processes (Fig. 10), it can be seen that the corrosion processes lead to an increase in the specific magnetization of up to 140 - 155 $A \cdot m^2 \cdot kg^{-1}$, and the transition temperature to the paramagnetic state to 840-1010 K. Most likely, this may be due to the intensive formation of Fe_3O_4 iron oxide on the surface of Nd-Fe-B thin layers, and even the presence of free iron ions upon heating the samples up to 1000 K during the specific magnetization measurements. This fact was demonstrated by the specific magnetization measurement and the accuracy of this measurement is very high. The presence of a free iron and Fe_3O_4 iron oxide is proveded by temperature dependences of specific magnetization. The determined from them Curie points of corroded films is about 1000 K, and as it is known that the transition temperature to the paramagnetic state of Fe_3O_4 oxide is in the range T_C ~ 820-860 K and of iron T_C ~ 1030 K. Only the release of these ions from the Nd-Fe-B thin layers may increase the specific magnetization value in comparison with non-corroded samples.

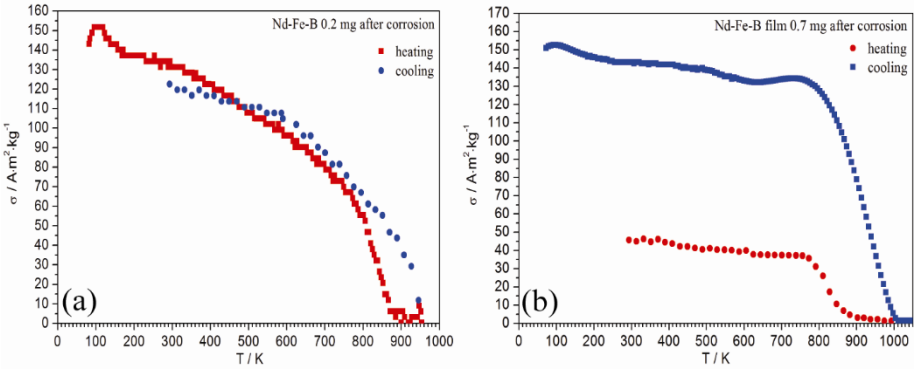

Figure 10. Temperature dependence of specific magnetization after corrosion action on Nd-Fe-B nanostructured thin films a) sample 1- 0.2 mg (sample 2- 0.3 mg has almost the same behaviour); b) sample 3- 0.7 mg.

In fact we can assume that $Nd_2Fe_{14}B$ is a rare-earth permanent magnet with a tetragonal structure. When exposed to NaCl solution (especially 3.5% NaCl, simulating seawater), it undergoes electrochemical corrosion, driven by the difference in electrochemical potential between the constituents: Nd (rare earth) is highly electropositive and oxidizes easily; Fe is moderately reactive; B is more inert but forms oxides slowly; Cl^- ions in NaCl solution accelerate corrosion by destabilizing protective oxide films. Neodymium ions dissolve into the electrolyte. These ions can react with water and hydroxide ions to form: Nd_2O_3 or $Nd(OH)_3$, which can precipitate locally as corrosion products. Iron in the lattice can also oxidized and form: Fe^{2+}/Fe^{3+}. Dissolved oxygen in NaCl solution reacts with water and electrons and generate OH^- and so the possibility of hydroxide formation. Chloride ions (Cl^-) are not directly oxidize, but destabilize oxides, facilitating Nd and Fe dissolution.

XPS measurements on all corroded nano-structured thin films (Fig. 11) proved the formation of those 2 species $Fe^{2+}(Fe_3O_4)$ and $Fe^{3+}(FeOOH)$. Decovolution data of Fe $2p_{3/2}$ spectra for the three studied samples, after oxidation during corrosion process, lead to a mixture of the oxides: Fe^{2+} (Fe_3O_4 with B.E. at 709.8, 710.2, 710.3 eV for the corresponding 3 samples 1, 2 and 3 respectively) and Fe $^{3+}$ (with BE at 711.2, 711.0, 711.2 eV for the corresponding 3 samples 1, 2 and 3 respectively). It has been previously reported that $Fe2p_{3/2}$ for Fe_3O_4 does not have a satellite peak [27, 28], and this is what we also observed in this study (Fig. 11a). Also, the very week satellite presented indicates the presence of an oxidized for of iron. It is absolutely possible (and common) for XPS peaks of Fe_2O_3, Fe_3O_4, and FeOOH to overlap, especially in the Fe 2p region. This overlap arises because all three compounds contain

Fe^{3+}, and their Fe $2p_3/_2$ binding energies fall in a narrow range: Fe_2O_3 710.6-711.2 eV, Fe_3O_4 709.5-710.6 eV and FeOOH 710.8-711.5 eV. So peak shapes can be nearly identical in typical lab-resolution XPS spectra and FeOOH [α (Lepidocrocite) or γ (Goethite)] can "hide" beneath the Fe_2O_3 signal. Using O1s high-resolution spectrum we could interpreting changes during Fe→FeOOH oxidation. In Fig. 11b the following peaks can be observed: Fe-O at 529.7 eV, Fe-OH at 531.7 eV and some absorbed species H_2O/-OH at 532.5-533 eV. The corroded surface shows oxide hydroxides that are very small in size and hydroxides that overlap in the XPS spectra over the oxides (see the very close binding energies) .So this proved that during corrosion of NdFeB in NaCl aqueous solution the oxidation can generate not only iron oxides but also hydroxide as presented in the XRD pattern (Fig.1e). Our results are in agreement with former publications [29,30]

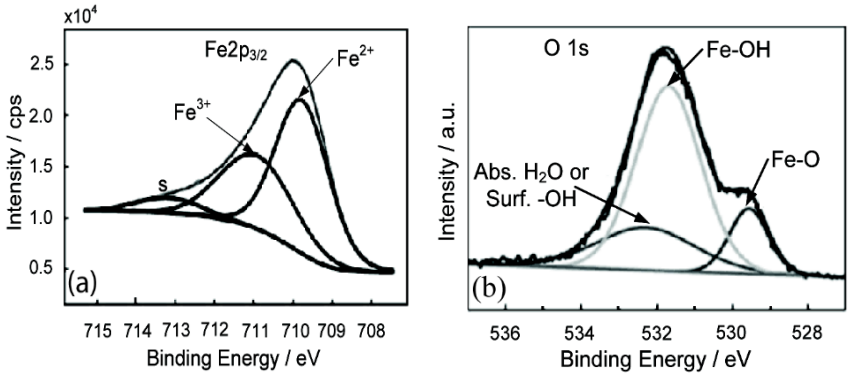

Figure 11. a) simulated XPS Fe2p3/2 spectra for Fe oxides and oxyhydroxides; b) simulated XPS spectra for O1s for Fe oxides/Oxihydroxides.

In Figure 12 are presented the XPS spectra: a) for the 3 NdFeB nano-samples after corrosion in 3.5 wt. % NaCl; b) high resolution spectra for Nd3d; c)deconvoluted spectrum for Nd3d.The presence of an oxygen phase (O at ~970 eV) is observed, which is due to the existence of the corrosion product $Nd(OH)_3$ [31]. On the overal spectra XPS the the Nd3d XPS peaks for Nd_2O_3 and $Nd(OH)_3$ can significantly overlap, because both compounds contain Nd in the +3 oxidation state. The main Nd peaks overlap within ~0.1–0.3 eV (982.4-982.5 eV for Nd_2O_3 and 982.5-982.7 eV for $Nd(OH)_3$, which is often within the instrumental resolution, especially in standard-resolution XPS. By capturing high-resolution Nd 3d and O 1s spectra, especially focusing on binding energies shifts, O-environment peaks, and satellite shapes, one can

confidently differentiate $Nd(OH)_3$ from Nd_2O_3. On the deconvoluted spectrum of $Nd3d_{5/2}$ (Fig.12 c) multiple split are observed. The peak at 980.7 eV confirms the presence of Nd^{3+} in hydroxide environment, similar to the values tabulated for $Nd(OH)_3$. This peak is smaller than the one corresponding to Nd_2O_3 (~983 eV) which proved that only some part of neodin oxide is transformed into hydroxide.

Also we have to take in account the spectrum of O1s from Fig. 11b which proved the existence of oxide and hydroxides after corrosion. The main peak between 530–531 eV, proved the metallic oxygen (Nd–O) while the shoulder at about 532 eV is due to hydroxyl groups, i.e. the OH in $Nd(OH)_3$.

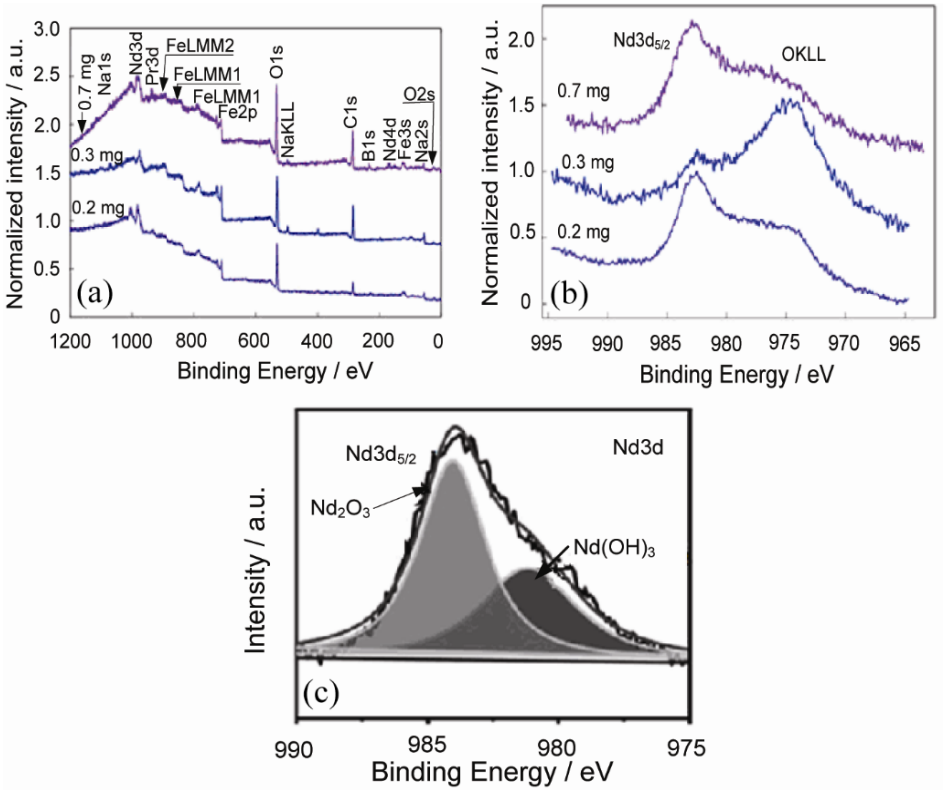

Figure 12. The XPS spectra obtained after corrosion of NdFeB thin films: a) the general spectra of the 3 films; b) the high-resolution spectrum of Nd3d; c) the deconvolution spectrum for Nd3d.

CONCLUSIONS

A method of producing $Nd_2Fe_{14}B$ thin films of different thicknesses at a nanoscale is developed.

X-ray diffraction study showed that synthesized films are nano-crystalline. SEM micrographs obtained on the Nd-Fe-B thin films deposited on glass revealed these films to be homogeneous and dense with a granulated surface texture, indicating a polycrystalline structure of equiaxed nanosized grains. The AFM images which measured the presence of Nd-Fe-B grains on the three thin films (with deposition weights of 0.2, 0.3 and 0.7 mg and and thicknesses of 40 nm,130 nm and 70 nm respectively) confirmed SEM observations that those samples are nano-structurated.

High-resolution XPS spectra showed that all elements constituting the nano-films are present in their oxidized forms (B_2O_3, Nd_2O_3, Fe_2O_3). SEM and AFM measurements of the samples after quick corrosion in a 3.5 wt. % NaCl solution revealed very significant morphological changes and confirmed the destruction of nano-films. The $\sigma = f(T)$ temperature dependences of specific magnetization revealed that after corrosion action on the thin films, their specific magnetization increases from 85 to 140 - 155 $A \cdot m^2 \cdot kg^{-1}$, and the transition temperature to the paramagnetic state increases from 620 to 840-1010 K. This behaviour could be explained by the intensive formation of Fe^{2+} oxide and presence of free iron ions on the surface of Nd-Fe-B thin layers. On a macro level, therefore, the magnetic properties of the thin Nd-Fe-B layers were determined not only by corrosion action on $Nd_2Fe_{14}B$ composition, but also by the formation of the Fe compositions and by free iron appearance. XPS analysis confirmed the presence of Fe_3O_4/FeOOH and of $Nd(OH)_3$ on the surface of the corroded samples.

EXPERIMENTAL SECTION

1. Thin film deposition of Nd-Fe-B

A powders, received from bulk commercially available Nd-Fe-B constant magnets (alloy MQP-B) (Magnequench Technology Center, SG, Singapore, Korea), was used as precursor in deposition of the samples. $Nd_2Fe_{14}B$ thin films were obtained by thermal evaporation (flash method) in a standard sputtering installation UHV-71R-2 type on 1 × 1 cm^2 glass substrates.The type of glass used was sodium-calcium-silicate (60-70% SiO_2, 12% Na_2O, 13% CaO, 2.8-4% MgO, 0.6-2% Al_2O_3); preliminarily a glass substrates were purified by liquid etching method. a special device based on shock vibration for a strictly dosed spilling powder charge into the evaporation zone is applied.

During deposition the powder grains fall on an tantalum evaporator, heated to a temperature significantly above the $Nd_2Fe_{14}B$ melting point (~ 1723 K – 1740 K), in this case, ~ 2773 K. Rapid evaporation and subsequent cooling of the substance deposited on the substrate maintains its composition and structure. By using this method, we obtained three different nanoscale films on glass substrate. Additionally, the films composition is confirmed by XPS analysis method. The thickness of received films is determinated by mass of the evaporated substance and by time of deposition, as following: 0.2 mg for 90 s (sample 1), 0.3 mg for 120 s (sample 2) and 0.7 mg for 300 s (sample 3). The films thickness will be specified below. All received films were transparent.

2.Thin film characterization

The crystalline structure of the as-deposited alloy thin films was characterized by X-ray diffraction (XRD) using an X-ray diffractometer (model DRON-2, Russia) WITH CU-Kα-radiation (λ = 0.154056 nm). X-ray patterns were obtained by the automatic recording of reflection intensities using a 0.03° scanning step and 2-3 s exposition time per step.

The morphology of the obtained thin films was analyzed before and after the corrosion process by scanning electron microscopy (SEM) using a 3d FEG apparatus equipped with an energy dispersive X-ray spectrometer (EDS). Atomic force microscopy (AFM) measurements were carried out in the non-contact mode with a XE-100 apparatus from Park Systems equipped with flexure-guided, cross-talked eliminated scanners, using sharp tips (<8 nm tip radius; Si material - PPP-NCLR type from NanosensorsTM) of app. 225 mm length, 38 mm width and 48 N/m nominal spring constant/~190 kHz nominal resonance frequency. The topographical 3D AFM images were obtained by scanning the AFM tip over areas of 8×8 μm^2 and 2×2 μm^2. XEI (v1.8.0) software program was used for displaying the images and subsequent statistical data analysis, including the calculation of the root mean square (RMS) roughness.

Surface analysis of the samples was performed by X-ray photoelectron spectroscopy (XPS) and was carried out on a Quantera SXM equipment, with a base pressure in the analysis chamber of 10-9 Torr. The X-ray source was Al K_α radiation (1486.6eV, monochromatized) operating at 350 W and the overall energy resolution is estimated at 0.65 eV by the full width at half maximum (FWHM) of the Au4f7/2 line. In order to take into account the charging effect on the measured Binding Energies (BEs), the spectra were calibrated using the C1s line (BE = 284.8 eV, C-C (CH)n bondings) of the adsorbed hydrocarbon on the sample surface.

The specific magnetization of Nd-Fe-B alloy thin films were measured by ponderomotive method in 0.86 T magnetic field and 80 - 720 K temperature range [32]. The method is based on, measurement of the sample force of retraction in magnetic field.

3. Corrosion assembly test

Electrochemical measurements of the thin Nd-Fe-B films magnets was studied experimentally by the potentiodynamic polarisation technique and using a potentiostat/gavanostat model PARSTAT 2273 (Princeton Applied Research, Oak Ridge, USA), with a “Power Corr” Software. For the electrochemical tests we used open circuit potential (OCP), linear polarization (LPR) and Tafel polarization measurements. These tests were performed in a 3.5 wt. % NaCl aerated aqueous solution under ambient conditions, (25 ± 2)° C and without stirring. All electrochemical tests were performed using a 100 cm^3 thermostatic glass cell with a standard three-electrode system, with the steel samples as the working electrode (WE), the Ag/AgCl reference electrode (saturated with 0.3 M KCl), and a platinum plate with area of 1 cm^2 as counter electrode, both produced by Radiometer (Radiometer Medical ApS., Denmark). The cell assembly was placed in a Faraday cage to prevent electrical interference.

ACKNOWLEDGEMENTS

This research was financed by Romanian Academy and Belarus Academy of Science bilateral project 2011-2013, no.F12RA-007 within the research programme “electrode processes, corrosion and materials for electrochemical systems” of the “Ilie Murgulescu” Institute of Physical Chemistry and by “EU(ERDF)-Romanian government” that allowed for acquisition of the research infrastructure under POS-CEEO 2.2.1 INFRANANOCHEM project nr.19 /01.03.2009. The authors thank prof. K. Yanushkevich[2(†)] for his guidance and help in the magnetism experiments. Authors also express sincere regret for prof. K. Yanushkevich passing into existence in 2023.

REFERENCES

1. *J. Thiel*sch; *D. Hinz;* L. Schultz*;* O.Gutfleisch; *J. Magn. Magn. Mat*., **2010**, *322*(20), 3208-3213. https://doi.org/10.1016/j.jmmm.2010.05.064
2. R. Sueptitz; K. Tschulik; M. Uhlemann; M. Katter; L. Schultz; A Gebert; *Corr. Sci*., **2011**, *53*(9), 2843-2852. https://doi.org/10.1016/j.corsci.2011.05.022

3. H. Sepehri-Amin; Y. Une; T. Ohkubo; K. Hono; M. Sagawa; *Scripta Mater.*, **2011**, *65*(5), 396-399. https://doi.org/10.1016/j.scriptamat.2011.05.006
4. W.F. Li; H. Sepehri-Amin; T. Ohkubo; N. Hase; K. Hono; *Acta Mater.*, **2011**, *59*(8), 3061-3069. https://doi.org/10.1016/j.actamat.2011.01.046
5. W.B. Cui; Y.K. Takahashi; K. Hono; *Acta Mater.*, **2011**, *59*(20), 7768-7775. https://doi.org/10.1016/j.actamat.2011.09.006
6. V.V. Ovchinnokov; *Mössbauer Analysis of the Atomic and Magnetic Structure of Alloys*, Cambridge International Science Publishers: UK, **2006**. ISBN: 1-904602-13-4
7. P. Gutlich; E. Bill; A.X. Trautwein; *Mössbauer Spectroscopy and Transition Metal Chemistry: Fundamentals and Applications,* Springer-Verlag: Berlin, Heidelberg, **2011**. ISBN: 978-3-540-88427-9
8. L.K.E.B Serrona; A. Sugimura; R. Fujisaki; T. Okuda; N. Adachi; H. Ohsato;I. Sakamoto; A. Nakanishi; M. Motokawa*; Mater. Sci. Eng.: B*, **2003**, *97*(1), 59-63. https://doi.org/10.1016/S0921-5107(02)00401-4
9. Y.G. Ma;Z. Yang;M. Matsumoto;A. Morisako;S. Takei; *J. Magn. Magn. Mater.*, **2003**, 267(3), 341-346. https://doi.org/10.1016/S0304-8853(03)00402-5
10. C. Constantinescu; N. Scarisoreanu; A. Moldovan; M. Dinescu; L. Petrescu; G. Epureanu;*Appl. Surf. Sci.*, **2007**, 253(19), 8192-8196. https://doi.org/10.1016/j.apsusc.2007.02.165
11. M. Ştefan; E.J. Popovici; I. Baldea; A. Mesaros; L. Muresan; R. Grecu; *Studia UBB Chemia*, **2006**, LI, 2, 147-151.
12. E. Burzo, *Studia UBB Chemia*, **2021**, LXVI, 3, 63-72. https://doi.org/10.24193/subbchem.2021.3.02
13. J.M. Song; *J. Korean Phys. Soc.*, **2001**, *39*, 314-317.
14. L.K.E.B. Serrona; A. Sugimura; N. Adachi; T. Okuda; H. Osato; I. Sakamoto; A. Nakanishi; M. Motokawa; D.H. Ping; K. Hono; *Appl. Phys. Lett.,* **2003**, *82*, 1751-1753. https://doi.org/10.1063/1.1561576
15. S.N. Piramanayagam; M. Matsumoto; A. Morisako; *J. Magn. Magn. Mater.*, **2000**, *212*(1-2), 12-16. https://doi.org/10.1016/S0304-8853(99)00597-1
16. PCPDFWIN, Joint Committee on Powder Diffraction Standards, International Centre for Diffraction Data, JCPDS-ICDD, v. 2.01, # 88-2285; 1998.
17. PCPDFWIN, Joint Committee on Powder Diffraction Standards, International Centre for Diffraction Data, JCPDS-ICDD, v. 2.01, # 74-1877; 1998.
18. PCPDFWIN, Joint Committee on Powder Diffraction Standards, International Centre for Diffraction Data, JCPDS-ICDD, v. 2.01, # 74-2195; 1998.
19. PCPDFWIN, Joint Committee on Powder Diffraction Standards, International Centre for Diffraction Data, JCPDS-ICDD, v. 2.01, # 83-2035; 1998.
20. A.M. Popescu; J. Calderon Moreno; K. Yanushkevich;A. Aplevich; O. Demidenko; E.I. Neacsu; V. Constantin; *J. Braz. Chem. Soc.* **2024**, 35, 1, e-20230089, 1-12. https://dx.doi.org/10.21577/0103-5053.20230089
21. S. Mao; H. Yang; Z. Song; J. Li; H. Ying; K. Sun; *Corros. Sci.*, **2011**, *53*(5), 1887-1894. https://doi.org/10.1016/j.corsci.2011.02.006
22. D.A. Shirley; *Phys. Rev. B,* **1972**, *5*, 4709-4714. https://doi.org/10.1103/PhysRevB.5.4709

23. J.F. Moulder; W.F. Stickle; P.E. Sobol; K.D. Bomben; *Handbook of X-ray Photoelectron Spectroscopy,* Physical Electronics USA, Inc., Chamhassen, **1995**.
24. R.J. Lad; V.E. Henrich; *Surf. Sci*., **1988**, *193*(1-2*)*, 81-93. https://doi.org/10.1016/0039-6028(88)90324-X
25. E. Paparazzo; *Appl. Surf. Sci*., **1986**, 259(1-2), 1-12. https://doi.org/10.1016/0169-4332(86)90021-8
26. P. Mills; J.L. Sullivan; *J. Phys. D-Appl. Phys.,***1983**, *16*(5), 723-732. https://doi.org/10.1088/0022-3727/16/5/005
27. D.D. Hawn; B.M. DeKoven; *Surf. Interface Anal.,***1987**, *10*(2-3), 63-74. https://doi.org/10.1002/sia.740100203
28. M. Muhler; R.Schlogl; G. Ertl; *J. Catal.,***1992**, *138*(2), 413-444. https://doi.org/10.1016/0021-9517(92)90295-S
29. A.P. Grosvenor; B.A. Kobe; M.C. Biesinger;N.S. McIntyre; *Surf. Interface Anal*. **2004**; 36: 1564–1574.DOI: 10.1002/sia.1984
30. C. Lyu;·L. Ju; X. Yang; L. Song; N. Liu; *J. Mater. Sci*., **2020**, *31,* 4797-4807. https://doi.org/10.1007/s10854-020-03041-2
31. S. Lasek; M. Kursa; K. Konecna; Proceeding of Metall Conference, **2011**, Brno, Cehia, p.1-5.
32. K.I. Yanushkevich; *Methods of specific magnetization and magnetic susceptibility measurement,* Assurance system of measurement uniformity of the Republic of Belarus, MVI. MN 3128-2009, BelSIM: Minsk, **2009**.